

## *Original*

Pein, J.; Valle-Levinson, A.; Stanev, E.V.:

### **Secondary Circulation Asymmetry in a Meandering, Partially Stratified Estuary**

In: Journal of Geophysical Research : Oceans (2018) AGU

DOI: 10.1002/2016JC012623

## RESEARCH ARTICLE

10.1002/2016JC012623

## Secondary Circulation Asymmetry in a Meandering, Partially Stratified Estuary

J. Pein<sup>1</sup> , A. Valle-Levinson<sup>2</sup> , and E. V. Stanev<sup>1</sup> <sup>1</sup>Institute of Coastal Research, Helmholtz-Zentrum Geesthacht, Geesthacht, Germany, <sup>2</sup>Department of Civil and Coastal Engineering, University of Florida, Gainesville, Florida, USA

## Key Points:

- Channel meanders transform along-channel flows into asymmetric secondary circulation and into turbulence
- At flood tidal phases, channel meanders enhance vertical mixing; at ebb phases, channel meanders enhance lateral currents
- Channel meanders tend to reduce the flood-directed transport of momentum and the extent of salinity intrusion

## Supporting Information:

- Supporting Information S1

## Correspondence to:

J. Pein,  
johannes.pein@hzg.de

## Citation:

Pein, J., Valle-Levinson, A., & Stanev, E. V. (2018). Secondary circulation asymmetry in a meandering, partially stratified estuary. *Journal of Geophysical Research: Oceans*, 123. <https://doi.org/10.1002/2016JC012623>

Received 12 DEC 2016

Accepted 13 JAN 2018

Accepted article online 25 JAN 2018

**Abstract** Numerical model experiments are used to study the effects of multiple channel bends on estuarine dynamics and, in particular, on secondary flows. These effects are demonstrated by comparing experiments with two different idealized trumpet-shaped estuaries, one straight and another one with a ~8 km meandering section in the middle of the estuary. Meanders complicate the flow field by introducing secondary processes. For instance, meanders increase turbulence and associated mixing locally within the water column, as well as outside the meandering portion. Furthermore, meanders transform up to 30% of the along-channel momentum into secondary circulation. Production of turbulence and secondary currents is different at flood and ebb tidal phases. At flood, meanders lead to unstable stratification and increased turbulence. At ebb, the flow develops a helical pattern and adjusts to the channel curvature with minimal decrease in density stability. The secondary circulation asymmetry is caused by an interplay between the across-channel baroclinic pressure gradient force and the centrifugal force. During ebb both forces enhance each other, whereas they oppose during flood. As a consequence of this interaction between baroclinic forcing and curving morphology, ebb flows and horizontal buoyancy fluxes increase relative to flood. The enhanced ebb dominance shifts a density front toward the mouth of the estuary, thus reducing salt intrusion.

## 1. Introduction

Channel curvature exists in most estuaries. It either stems from submerged river meanders, which is the case in the southern North Sea, or is generated by coastal morphological processes (Ahnert, 1960; Marani et al., 2002). Another basic shape that characterizes most estuaries is the coastline convergence. Curvature and convergence often appear in the same area but one of them could dominate the local physical processes depending on the regional situation. Estuarine convergence can explain tidal amplification, generation of over-tides and reflection of a tidal wave (Aubrey & Speer, 1985; Friedrichs & Aubrey, 1988; Giese & Jay, 1989). Winterwerp (2011) attributed the reflection of a tidal wave to channel curvature. Often the specific effects of channel convergence and channel curvature may be difficult to discern. That is why the isolated effects of channel curvature deserve additional scrutiny.

Simplified models have been used as a first approximation to analyze complex problems such as those outlined above. Several authors have implemented 1-D models to examine idealized along-channel dynamics, or 2-D models resolving also the vertical structure along a basin forced by tides (Friedrichs et al., 1998; Talke et al., 2009). Channel curvature and its associated secondary flows are customarily neglected in the 1-D and 2-D models.

Secondary circulation is known as the flow that emerges perpendicular to the principal-axis flow (Rozovskii, 1957). The principal-axis flow is usually drawn from the vertically averaged flow in a single velocity profile (Geyer, 1993). Differential advection of salinity and Coriolis deflection drive currents normal to the principal-axis flow, in addition to channel curvature (Dronkers, 1996). In addition, secondary currents are controlled by advection of lateral momentum (Nidzicko et al., 2009) and by bottom and internal friction (Becherer et al., 2015).

A formal analytical framework to study secondary circulation has been presented by Kalkwijk and Boij (1986) who quantified lateral flows on the basis of Coriolis force and curvature. Although their work was

aimed at providing a framework for two-dimensional (2-D) secondary flows, it has served as reference for three-dimensional (3-D) studies of secondary circulation (Buijsman & Ridderinkhof, 2008; Lacy & Monismith, 2001; Nidziko et al., 2009; Seim & Gregg, 1997). Some authors have also investigated the feedbacks between main flow and secondary flow. Geyer (1993) demonstrated that increased vertical shear of the along-channel flow enhances the curvature-induced secondary circulation. Seim and Gregg (1997) emphasized the importance of curvature for bed shear stress to be distributed throughout the flow field. Becherer et al. (2015) demonstrated that lateral flows contribute to estuarine exchange flow in a tidal inlet, using a theoretical framework based on vorticity. The above studies focus on observations and are necessarily limited to a single or a few locations. Our aim is to widen the scope of those studies, by considering the estuary as a whole, in order to enable a comparison between different estuarine flow regimes. A modeling study of secondary circulation was presented by Lerczak and Geyer (2004), who demonstrated the interactions between along-channel dynamics, stratification, and the cross-channel balance in a straight channel. Purkiani et al. (2015) revealed the crucial role of advection of lateral density gradients for the onset of stratification in a tidal inlet with channel curvature. The present study concentrates on the effects of multiple channel bends in enhancing the primary circulation as well as the cross-channel dynamics.

We compare the along-channel and cross-channel dynamics in a straight and a meandering estuary, and examine the along-channel momentum in the areas of channel meanders. Here the most relevant question is how the along-channel momentum transforms into secondary circulation and to what degree the kinetic energy is reduced by mixing processes.

## 2. Methods

### 2.1. Model

This study examines the hydrodynamics derived from a 3-D unstructured numerical model, SCHISM, the Semi-implicit Cross-scale Hydroscience Integrated System Model (Zhang et al., 2016), which was derived from the Semi-Implicit Eulerian-Lagrangian Finite-Element model SELFE (Zhang & Baptista, 2008). It is based on the Reynolds-Averaged Navier-Stokes equations in Cartesian coordinates. The model has been extensively validated for the Ems estuary (Pein et al., 2014). To study secondary circulation, we use two idealized estuaries. The first estuary is a straight channel of 100,150 km length and 12 km width at the mouth (Figure 1a). The channel width decreases exponentially and equals 100 m at the head of the estuary. The depth decreases linearly with a rate of 0.27 m/km between 0 and 30 km of the estuary, and 0.11 m/km between

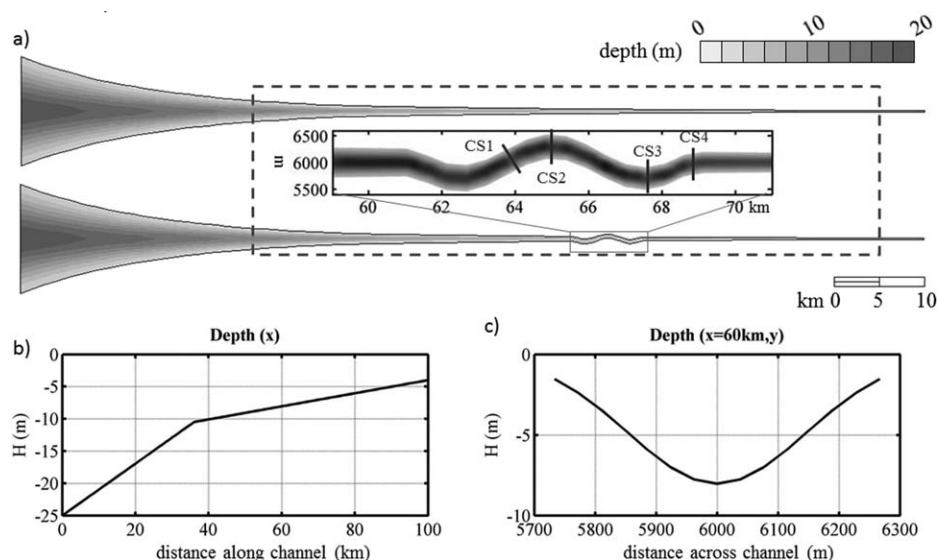


**Figure 1.** (a) Model bathymetry of the idealized straight and meandering estuaries; (b) depth along the channel's axis; (c) cross-sectional bathymetry. The region of analysis is delineated by the dashed lines in Figure 1a. The small plot in the middle of Figure 1a gives a zoomed-in view of the meandering region with the black bars indicating the positions of cross-sectional profiles (CS1, CS2, CS3, and CS4) analyzed in the remainder of the paper.

30 km and the landward boundary (Figure 1b). The length and width of the channel as well as the change of the bottom slope between the outer estuary and its middle and upper reaches were inspired by the dimensions and shape of the Ems estuary. Across the channel, the bathymetry has a Gaussian shape with the deepest part of the channel located in the middle of the cross section (Figure 1c).

The bathymetry of the second estuary is the same as the first one but with a sinusoidal perturbation of the channel's  $y$ -coordinate (coastline) resulting in a meandering section with three bends between 61 and 69 km of the estuary (Figure 1a). The length of the channel axis of the meandering channel is the same as the length of the straight channel. The radius of curvature of the meanders amounts to 2,500 m, which corresponds to the radii found in the Ems estuary of the German Wadden Sea. We chose three bends because (1) a meander consists at least of two bends and (2) adding a third bend allows us to examine the secondary flows in the middle bend ensuring symmetry for flood and ebb flows.

The model domain is resolved by an unstructured triangular grid. The grid resolution ranges between 2,000 m at the seaward open boundary and 10 m at the landward open boundary. Both the straight and the meandering channel experiments are forced by a M2 tide at the seaward open boundary. River inflow at the head amounts to 80 m<sup>3</sup>/s. Salinity is initialized with a constant gradient of 0.3 g/kg/km, ranging from 30 g/kg at the mouth to 0 g/kg at the landward boundary. These values are kept constant at the model boundaries during model integration. Temperature values are kept constant at 15°C throughout the estuary and their effects on the dynamics are neglected. The spin-up time of the model is 28 days (see supporting information for detailed information of the spin-up, Figure S3) and the results discussed in this paper focus on the two tidal cycles following day 28 of the simulation. The overall design of the idealized cases aims to emulate the conditions at the Ems estuary, i.e., to represent a partially stratified mesotidal estuary. The Coriolis force is disabled to allow for the straightforward identification of curvature-induced centrifugal force. As shown by Kalkwijk and Booij (1986), the curvature-induced lateral flow scales with the square of the main flow.

## 2.2. Analysis

For the analysis of the model output, we consider a coordinate system with a streamwise coordinate  $s$  and a coordinate  $n$  normal to  $s$ . In this coordinate system, the lateral currents as a function of depth  $z$  are approximated as (Kalkwijk & Booij, 1986; Lacy & Monismith, 2001; Nidzieko et al., 2009):

$$\frac{\delta u_n}{\delta t} = \frac{u_s^2 - u_s'^2}{R} - \left( u_s \frac{\delta u_n}{\delta s} - u_s' \frac{\delta u_n'}{\delta s} \right) - \frac{g}{\rho_0} \left( \int_z^\eta \frac{\delta \rho}{\delta n} dz' - \int_z^\eta \frac{\delta \rho'}{\delta n} dz' \right) + \left( \frac{\delta}{\delta z} \left( A \frac{\delta u_n}{\delta z} \right) + \frac{\tau}{\rho H} \right), \quad (1)$$

where the term on the left-hand side is the local rate of change of the lateral horizontal current  $u_n$ . The first term on the right-hand side refers to the curvature-induced centrifugal force with the overbar denoting vertical averages. The second term is the along-channel advection of lateral momentum. The third term is the baroclinic pressure gradient force with gravity constant  $g$ , reference density  $\rho_0$ , and water level  $\eta$  as well as local density  $\rho$ . Finally, the fourth term is the stress divergence (or friction) with eddy viscosity  $A$ , bottom shear stress  $\tau$ , and overall water depth  $H$  (Nidzieko et al., 2009; Seim & Gregg, 1997). In the following, we refer to equation (1) as the "lateral momentum equation."

## 3. Results

The results section is structured as follows: in section 3.1, we compare general features of the tidal range, tidal flow, and salinity fields in a straight and in a meandering channel. In section 3.2, we examine the across-channel momentum balances, concentrating on the meandering case.

### 3.1. Intercomparison Between Straight and Meandering Channels

#### 3.1.1. Along-Channel Change of Tides

The straight and the meandering idealized estuaries differ in that the meandering case has three bends between 61 and 69 km (Figure 1; see section 2.1). The maximum deviation of the meandering channel axis from the straight channel axis (290 m at 65 km) slightly exceeds half the width of the channel (230 m at 65 km).

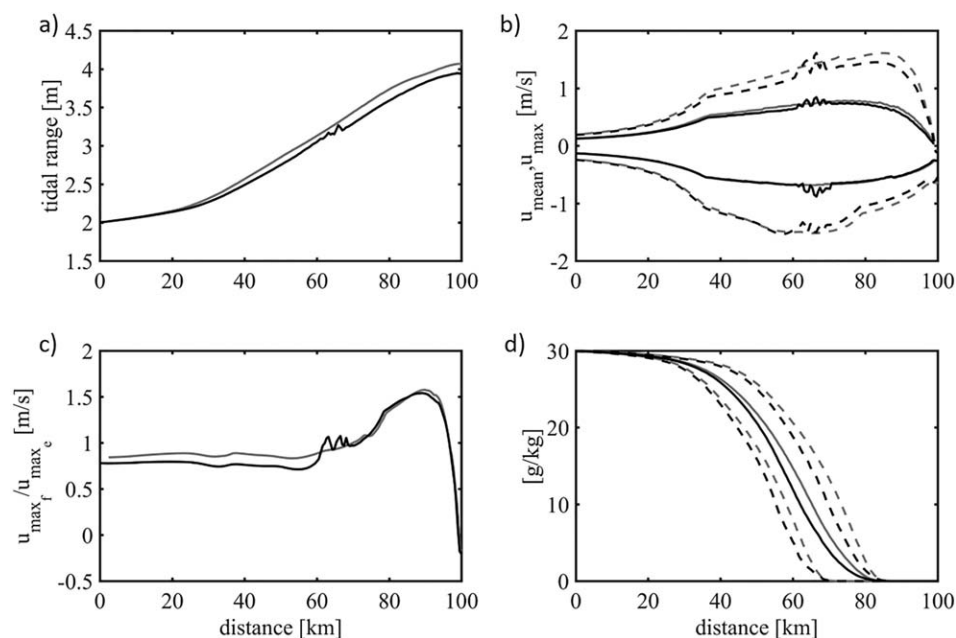


**Figure 2.** (a) Tidal range (m) along the channel axis of an idealized straight, funnel-shaped estuary (gray line) and an idealized meandering estuary (black line). (b) Solid lines: cross-sectionally averaged and time-averaged flood and ebb along-channel velocities (flood is positive); dashed lines: cross-sectional maximum velocities. (c) Ratio between maximum flood and maximum ebb surface velocity (tidal current asymmetry). (d) Solid lines: the tidally averaged surface salinities; dashed lower lines: minimum surface salinities; and dashed upper lines: maximum surface salinities.

Both model setups result in a tidal range increasing from 2 m at the mouth of the estuary to approximately 4 m at its head (Figure 2a). These ranges are comparable to those observed in the Ems estuary, which inspired the design of the idealized morphologies (Pein et al., 2014). The tidal amplification is higher in the straight channel, exceeding the range in the meandering domain by 0.05 m around 35 km and by 0.15 m at the estuary head. Over the meandering section the range reduces by several centimeters from bend to bend. A similar reduction happens with the tidal velocities (Figure 2b). Therefore, the primary effect of the meanders is to increase friction. This results in a general damping of the tidal wave and tidal currents.

Tidal range and flows have different distributions throughout the estuary when comparing straight and meandering configurations. Along-estuary differences arise because the processes associated with the meanders are nonlocal and cause contrasting changes from flood to ebb. The time-averaged ebb velocities of both configurations are practically the same except within the meandering section (Figure 2b). Maximum ebb flows decrease locally in the meanders and also landward of the meanders. Maximum flood flows decrease almost throughout the estuary under the meandering configuration. It is evident that the flood and ebb flows respond differently to the modification by the meanders. This finding is quantified by the ratio of maximum flood and ebb surface velocities, i.e., the tidal current asymmetry (Figure 2c). Both cases reveal ebb-dominant conditions ( $\max(u_{\text{flood}})/\max(u_{\text{ebb}}) < 1$ ) in the seaward half of the estuary and flood-dominant conditions ( $\max(u_{\text{flood}})/\max(u_{\text{ebb}}) > 1$ ) toward the head of the estuary. However, ebb dominance is enhanced seaward of the meanders in the meandering case. This ebb dominance occurs because the ebb currents seaward of the meanders do not slow down despite the meander-induced friction (Figure 2b). Detailed examination of the lateral circulation in section 3.2 reveals that the interaction between density gradients and the curving topography leads to such asymmetry. In the supporting information we present results with the same two configurations but under homogeneous water density (supporting information Figures S1 and S2). Homogeneous results demonstrate that without density gradients, the reduction of flood and ebb currents is almost identical. Inclusion of density gradients results in the meanders having a greater impact on the dynamics than under homogeneous conditions.

The meanders' influence on salinity is illustrated by the differences in the area between the minimum and maximum surface salinity along the channel axis (Figure 2d). In both the straight and the meandering

estuary, the minimum, maximum and tidally averaged salinities show a sigmoidal curve typical of real estuaries (Monismith, 2010; Talke et al., 2009). Meanders hinder saltwater intrusion by shifting the average position of the salinity front by approximately 3 km toward the ocean. The tidal excursion of the zero isohaline (tip of the salinity front) becomes slightly shorter. In the meandering case the tip of the salinity front moves back and forth between 70 and 85 km, i.e., landward of the meanders. The tidal excursion in this region is thus approximately 15 km; the channel meanders are at the landward end of the salinity front. In this region, the flow is constantly stratified although stratification and velocity shears vary over the tidal cycle.

### 3.1.2. Vertical Structure of Tidal Flow

Meanders also modify the internal structure of the flows, as illustrated by along-estuary sections during flood and ebb (Figures 3a–3d). Flood currents decrease in the meandering configuration as far as 15 km before they reach the first bend and as far as 20 km in the landward direction (Figure 3c versus Figure 3a). This further illustrates the finding that the meander-induced attenuation of tidal currents extends over a portion of the estuary that is larger than the scale of the meanders themselves. Locally the meanders increase the vertical shear of the along-channel flood velocity (Figure 3c versus Figure 3a). At ebb, the meanders favor mixing of along-channel momentum from the surface to the bottom. This is shown by the isolines of vertical shear appearing closer to the channel bed in the meandering configuration than in the straight configuration (Figure 3d versus Figure 3b, 60–70 km). As a consequence, the internal current asymmetry between flood and ebb along-channel flows decreases in the meandering configuration, i.e., increased shears develop in ebbs (Figures 3c and 3d versus Figures 3a and 3b). In both phases of the tidal cycle, near-bottom currents are greater in the meandering configuration than in the straight channel. Thus, the presence of meanders lessens the differences between flood and ebb along-channel flows (see also supporting information Figure S1). The reduction in tidal current asymmetry in the meandering configuration may be attributed to two processes: (1) reduction of flood currents but not of ebb currents seaward of the meanders and (2) increased mixing of the ebb currents over a greater portion of the water column in the meandering region. Outside of the meandering region the internal asymmetry between flood and ebb flow, i.e., the weakly sheared flood versus the strongly sheared ebb, remains essentially unchanged.

Along-channel sections of turbulent kinetic energy (TKE) reveal increases induced by the meanders (Figures 3e–3h). In both the straight and the meandering channel, TKE has minima at the surface and maxima near the bed. Also, both configurations exhibit higher TKE at flood than ebb, underscoring the internal asymmetry described by the horizontal velocities (Figures 3a–3d). In the straight channel, the longitudinal TKE maximum corresponds to the regions of strongest flood and ebb currents, around 80 km for flood and 65 km for ebb. In the presence of meanders, the location of the TKE maximum is completely determined by the region of channel curvature (between 60 and 70 km). Both flood and ebb see TKE increase, locally reaching levels not existing in the straight channel even at the time of maximum flood. Outside the meandering section, on the contrary, TKE levels seem to decrease slightly in flood. However, elevated TKE in the seaward reaches at ebb indicates that the meanders modify the properties of ebb flows not just locally.

A closer look at the consequences of the flow asymmetries is determined by the competition between mixing and stratification. Along-channel profiles of the log gradient Richardson number ( $Ri$ ) on flood and ebb are shown in Figures 3i–3l.

The higher TKE induced by the meanders hinders stratification locally, which is demonstrated by both  $Ri$  and salinity contours. In both model configurations,  $Ri$  shows higher values at flood than at ebb. The fields portrayed in Figure 3 represent snapshots of the estuarine dynamics during maximum tides so that flood works against stratification, which is overcome only toward the end of flood. In contrast, ebb flow tends to establish stratification, which attains its maximum only toward the end of ebb (see a Hovmöller diagram of stratification in supporting information Figure S5). In the meandering configuration, flood currents completely break down stratification and enhance local instabilities (Figure 3k). The value of  $Ri_c = 0.25$ , which is reported in the literature as a critical value, is shown in these figures by the white contour line. At ebb, the local effect of the meanders on stratification is clearly weaker than on flood (Figure 3l). The 10 g/kg isohaline, for example, remains slightly slumped over during ebb in the meandering configuration (compare Figure 3l and Figure 3k), demonstrating that the vertical mixing is not complete.  $Ri$  remains above the critical value in the bends of the meandering section (63, 65, and 67 km in Figure 3l). Out of the meandering section, especially in the seaward reaches of the estuary, both  $Ri$  and the isohalines indicate increased stratification for flood and ebb in the meandering configuration (Figures 3k and 3l versus Figures 3i and 3j). This

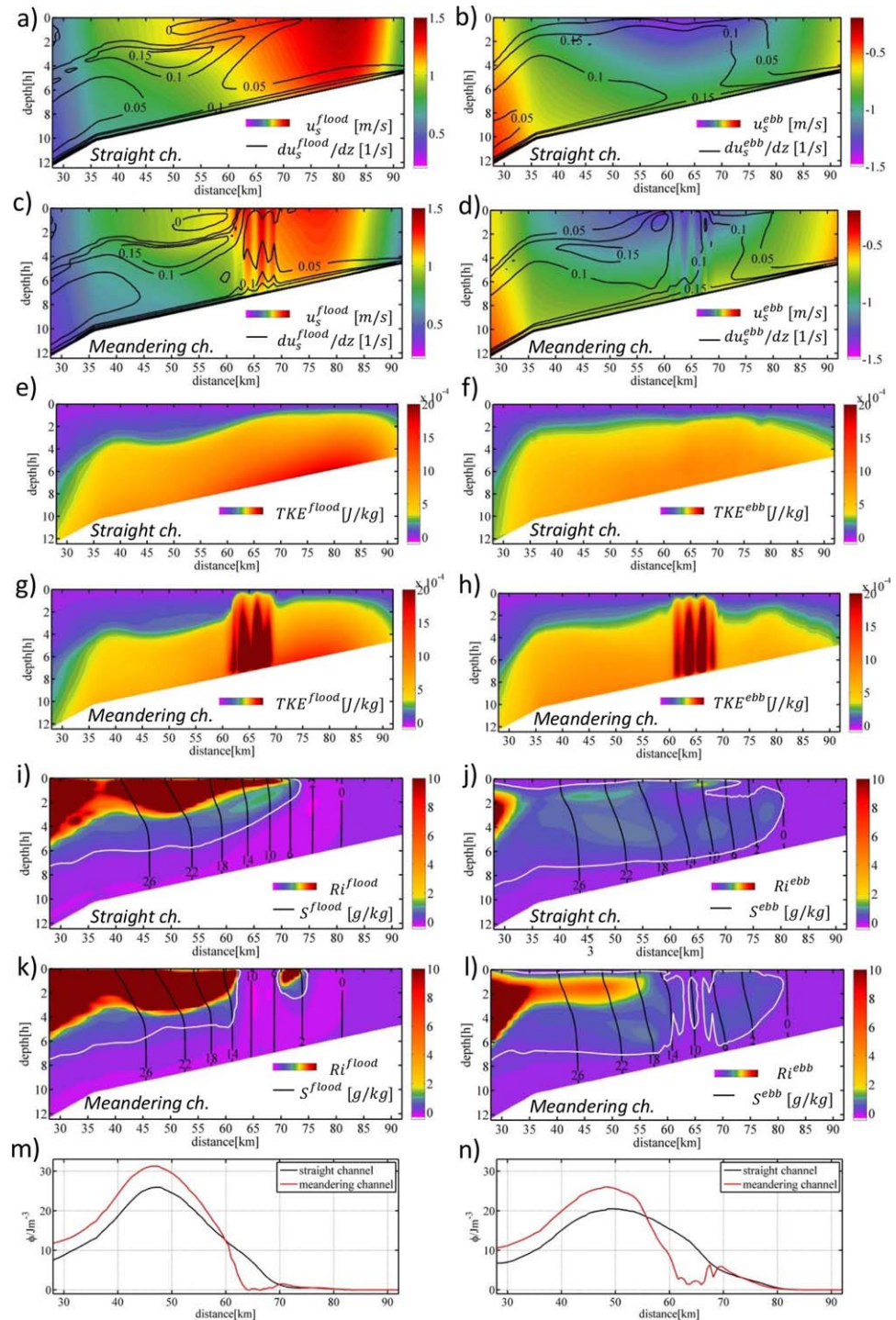


**Figure 3.** Along-channel sections of some variables in (a, b, e, f, i, j) a straight and (c, d, g, h, k, l) a meandering estuary at (left) flood and (right) ebb. The width-averaged along-channel velocity (m/s) is given for (a, c) flood and (b, d) ebb along the channel axis of (a, b) a straight and (c, d) a meandering estuary, respectively (see Figures 1b and 1c). The contour lines illustrate the vertical shear of the along-channel velocity, i.e.,  $du_s/dz$  ( $s^{-1}$ ). The turbulent kinetic energy ( $m^2/s^2$ ) is presented for (e, g) flood and (f, h) ebb along the channel axis of (e, f) a straight and (g, h) a meandering estuary, respectively (see Figures 1b and 1c). Further illustrated is the gradient *Richardson* number for (i, k) flood and (j, l) ebb along the channel axis of a straight (i, j) and a meandering (k, l) estuary, respectively (see Figure 1b, c). Here the black contour lines represent the salinity field at times of full flood and ebb, respectively. The white contour line delineates  $Ri_c$ . The bottom plots show the vertically integrated potential energy anomaly ( $J m^{-3}$ ) at (m) flood and (n) ebb. The timing of full flood and ebb is defined as the times of maximum currents at 60 km in the two experiments (Figure 1a).

result is congruent with the associated retreat and steepening of the salinity front in the meandering configuration (Figure 2d).

These findings are supplemented by potential energy anomaly  $\phi$  values, a proxy for stratification, calculated along the *thalweg* of the straight and meandering configurations (Figures 3m and 3n; see also Hovmöller diagrams of  $\phi$  covering two tidal cycles, in supporting information Figure S5). According to Simpson et al. (1981) and Burchard and Hofmeister (2008),  $\phi$  in estuaries is defined as  $\phi = -1/H \int_{-H}^{\eta} gz(\hat{\rho} - \rho) dz$ , where  $\eta$  is the sea surface elevation and  $\hat{\rho}$  is the vertically averaged density. Positive values of  $\phi$  indicate stable stratification, while negative  $\phi$  values denote unstably stratified conditions;  $\phi$  is zero when the water column is completely mixed. Both configurations have their maximum  $\phi$  permanently in the middle reaches between 45 and 60 km, with values decreasing toward the open boundaries. Values of  $\phi$  reveal different along-channel distributions from flood to ebb. At flood,  $\phi$  is maximum around 45 km with values decreasing steeply in both directions (Figure 3m). At ebb, maximum  $\phi$  is smaller but is enhanced in the upper reaches toward the tip of the salinity front (Figures 3n and 2d). Meander processes reduce  $\phi$  locally. At flood, the reduction starts at the entrance of the meandering section. At around 65 km (this location corresponds to CS2 in Figure 1a)  $\phi$  falls slightly below zero indicating that meander-induced mixing homogenized the water column. At ebb, the effect of the meanders is similar but the stratification is not completely suppressed by meander-induced mixing (between 61 and 69 km in Figure 3n). On the other hand, meanders increase stratification at ebb just landward and slightly seaward from the meandering section (Figure 3n). Thus meanders enhance the transport of buoyancy during ebb leading to enhanced stratification outside the meanders (see also the general changes in  $\phi$  due to the meanders in supporting information Figure S5a–S5c). The local reduction of  $\phi$  induced by the meanders leads to a local increase of potential energy. Seaward of the meanders,  $\phi$  increases and thus potential energy is reduced (see also velocities in Figure 2b and Figures 3a–3d).

### 3.1.3. Lateral Flow

Tidally averaged, or subtidal, along-channel currents illustrate the estuarine exchange flow in the straight configuration (Figure 4a). The subtidal velocities exhibit a classical density-driven circulation with inflow near the bottom and outflow near the surface. In the straight configuration, the exchange flow pattern (55–65 km in Figure 4a) displays a maximum top-bottom difference of 0.35 m/s in the region of the maximum longitudinal salinity gradient (55–65 km in Figure 2d). The meanders cancel out exchange flow locally as seen from the differences between subtidal along-channel currents in the meandering and in the straight channel cases (Figure 4b). Suppression of exchange flow colocalizes with the area of the meanders and with the region where tidally averaged salinity experiences the greatest reduction (between 55 and 70 km in Figure 4b). Landward of the meanders, vertical isolines of salinity difference confirm that the baroclinic regime has been weakened or eliminated in this region. In contrast, the tilted isolines seaward of the meanders reveal increased tidally averaged stratification (30–55 km in Figure 4b). Thus, the density-sensitive regime has migrated seaward because of the meanders. The major effects of the meanders summarize as follows: (1) reduction of the tidal range and tidal currents, (2) increase of ebb dominance and exchange flow in the seaward reaches, (3) reduction of exchange flow in the meandering section, and (4) overall reduction of salinity intrusion. In the following, we describe the lateral flows, which are crucial for the meander-induced modifications of the longitudinal and vertical fields (Figures 2–4).

In both configurations, the tidally averaged lateral flow in the lower reaches (i.e., away from the bends in the meandering case) consists of two symmetrically oriented cells with flow toward the channel central axis at middepth and a compensating flow toward the channel sides at the bottom (Figures 4c–4f). This pattern is consistent with the transverse circulation arising due to the differential advection of salinity during the flood period (Nunes & Simpson, 1985). Also in both cases lateral currents are about one order of magnitude weaker than along-channel currents (see the differences in the color coding of individual plots in Figures 4c–4f). At the edge of the salinity front, 72 km of the straight configuration, lateral currents indicate convergence over the middle of the channel, which can be seen from northward flow in Figure 4c and to the south in Figure 4e. With the meanders, the differential advection of salinity becomes asymmetrical about the *thalweg* destroying the convergence over the middle of the channel (landward from 70 km in Figures 4d and 4f). Seaward of the meanders, the three-layer lateral circulation pattern is slightly enhanced due to the meanders (25–55 km in Figures 4c–4f). At the bends, the across-channel circulation is indicative of unidirectional helical cells (Figures 4d and 4f) with lateral currents increasing more than twice compared to the

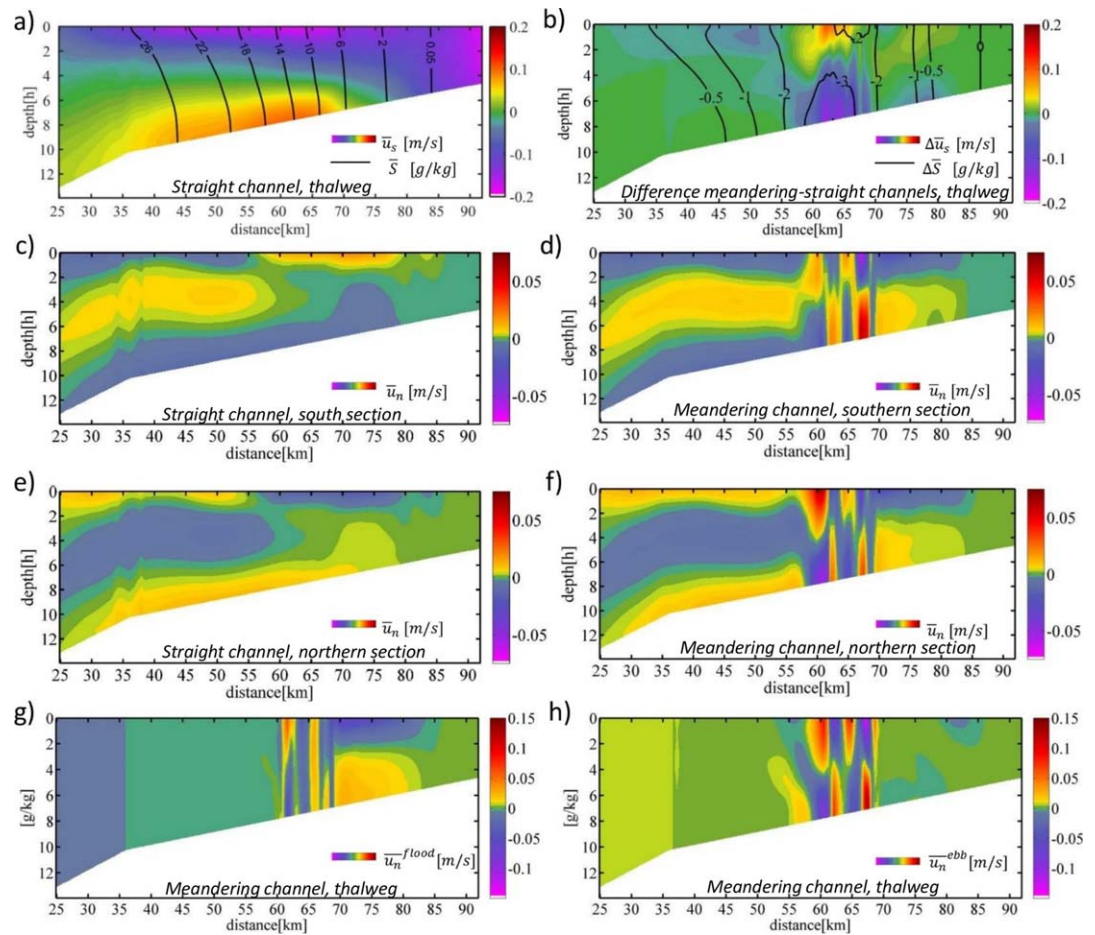


**Figure 4.** (a) Tidally averaged along-channel velocity (m/s) plotted along the channel axis of a straight estuary. (b) Tidally averaged along-channel velocity (m/s) along a section following the axis of a meandering estuary minus the tidally averaged velocities shown in Figure 4a. The tidally averaged lateral velocity (m/s) along a section half-way between the axis and the (c, d) southern and (e, f) northern coast is also given for (c, e) the straight and (d, f) the meandering estuary. The tidally averaged isolines of salinity (g/kg) are also plotted in (a) the straight estuary and (b) the isolines of the tidally averaged salinity difference between the meandering estuary and the straight estuary. The lateral velocity (m/s) averaged along the lateral sections and time-averaged for one tidal period over (g) flood and (h) ebb, where flood (ebb) has been defined as the times when local currents are flood-directed (ebb-directed).

symmetric flow in the straight channel (Figures 4c and 4e). From bend to bend, the circulation cells change their sense of rotation, which is in agreement with theory of flow in curved channels (61–69 km in Figures 4d and 4f). Theory predicts flow in the top layer toward the outside of the bend and recirculation at the bottom toward the inner bend (Rozovskii, 1957). At the entrance to the meandering section the tidally averaged lateral flow forms a cell that stretches several kilometers seaward between 55 and 61 km (Figures 4d and 4f). This circulation cell on the one hand restratifies the water column, which can clearly be seen from the enhanced  $Ri$  between 55 and 60 km in flood and ebb tidal phases (see Figures 3k and 3l). On the other hand, the enhanced residual lateral flow affects the along-channel exchange flow because of the coupling between longitudinal and lateral currents (see the discussion of Figure 6c in section 3.2.1). As a consequence, the tidally averaged along-channel flow reveals intensified outflow in the meandering channel of 5 cm/s (see 50–55 km near surface in Figure 4b).

In the meandering channel, the lateral currents are greater during ebb than during flood, indicating an asymmetry of the generation or control of secondary circulation during the two tidal phases (Figures 4g and 4h). The lateral ebb currents indicate clear overturning whereas flood currents show nearly depth-independent lateral flow conditions. Such a difference between flood and ebb lateral flows is remarkable because the along-channel patterns of Figure 3 suggest that the meanders tended to reduce typical

differences between flood and ebb. This is explained by the shift of the position of the greatest vertical shears of along-channel flow toward the channel bed at ebb (Figures 3b and 3d). Because of this shift, which is caused by the meanders, patterns of along-channel flow at ebb approach the ones emerging during flood (Figure 3c). A similar change happens to the pattern of  $Ri$  at ebb. Between 60 and 70 km meanders bring about subcritical levels of  $Ri$  several meters above the channel bed (Figure 3i). Also at ebb and in the lower reaches (seaward from 55 km), meanders lead to elevated stratification ( $Ri > 2$ , Figure 3l versus Figure 3j). Both, the unstable stratification between 60 and 70 km and the elevated stratification in the lower reaches were indicative of flood in the straight channel configuration (Figure 3i), but with the meanders they emerge at both periods of the tidal cycle. The lateral ebb flows reveal a fully developed three-dimensional flow regime that does not appear in a straight channel. Outside the meandering section the typical structure for straight channel flows remains practically unchanged: lateral flows are greater in flood than in ebb (70–85 km in Figures 4g and 4h; supporting information Figure S6; see also Lerczak & Geyer, 2004).

### 3.2. Lateral Dynamics in Meandering Channels

#### 3.2.1. Asymmetric Lateral Circulation

It follows from the first and third terms on the RHS of equation (1) that the secondary circulation results from along-channel momentum and from lateral density gradients deviating from their vertical averages. One process leading to lateral variations of along-channel flow is differential advection, which arises over a cross-sectional bathymetry with deep *thalweg* and shallow flanks (Nunes & Simpson, 1985). Differential advection must also be active in driving secondary flows in the configuration of the experiments presented here because of the Gaussian shape of the cross-sectional bathymetry. However, it is unclear how differential advection, which is symmetric in straight channels, is affected by channel curvature and multiple meanders. The impact of channel curvature on along-channel advection will be crucial for the forcing of the lateral circulation. Locally, meanders lead to lateral and along-channel gradients of the along-channel currents  $du_s/dx$  (Figures 5a and 5c). Analogous to flow in a straight channel, the strongest currents tend to flow through the meanders as straight as possible. This is why along-channel flows decrease from the inner bend to the outer bend in the meanders (Figures 5a and 5c). In following their trajectory, along-channel flows necessarily deviate from the *thalweg* (which is not straight). Approaching the channel walls the high momentum flow induces increased TKE (see Figures 3g and 3h). The small depth at the channel sides does not allow the fastest currents to emerge directly at the channel wall so that the currents core of maximum flow occurs between the inner side of the bend and the *thalweg* (Figures 5a and 5c). In consequence, the mechanism of differential advection becomes asymmetrical about the *thalweg*, transporting momentum

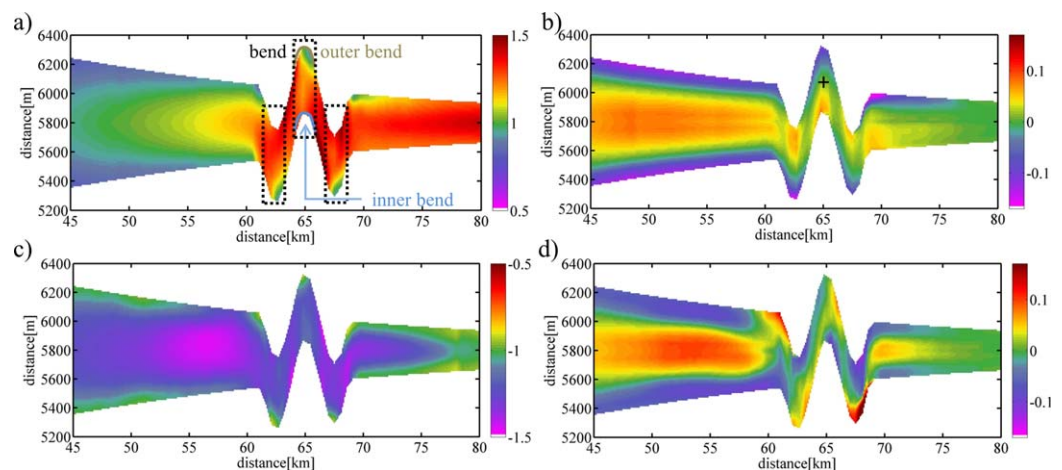


**Figure 5.** (a, c) Along-channel surface velocity (m/s) and (b, d) anomaly of salinity from its cross-sectional average (g/kg) are given for (a, b) maximum flood and (c, d) maximum ebb along a meandering idealized estuary. The dashed rectangles identify the regions of the channel which in the text are named “bends.” As an example, the inner bend and the outer bend are indicated for the middle bend. The cross in Figure 5b marks the profile location analyzed in Figure 6. The aspect ratio is chosen different from the one in Figure 1 in order to better visualize the patterns in the meandering part of estuary.

and tracers at a greater rate near the inner bends. At flood, the increased advection near the inner bend is associated with generation of a negative salinity gradient between the inner side of the curve and its outer side. This gradient tends to be further enhanced by the upwelling of salinity near the inner bends during times when the lateral currents are controlled by the curvature-induced forcing. At ebb, the increased advection near the inner bend leads to a positive gradient of salinity with relatively fresher water at the inner bend and the salinity maximum emerging near the outer bend (Figures 5c and 5d).

Between single bends, the flow is (1) stronger than in the bends and (2) more symmetrical about the channel axis (Figure 5a). The first point implies that the flow loses momentum in the bends either to secondary circulation or to TKE. Deceleration happens especially in the outer bends where currents locally decrease by up to 30%. The resulting “pockets” of slow flow hinder the advection of momentum or tracer, and setup gradients between the outer bend and the inner bend. Accordingly, lateral salinity gradients emerge in the channel bends (Figures 5b and 5d). Similar to the tidally averaged lateral velocity (Figures 4d and 4f), these gradients alternate in direction from bend to bend (Figures 5b and 5d). They also change sign between flood and ebb, i.e., the denser water concentrates at the inner bends during flood and at the outer bends at ebb (Figures 5b and 5d). The local lateral salinity gradient thus appears as a consequence of the interaction between the bathymetry and the tidal currents with horizontal density gradients. It is evident then that channel curvature modifies the differential advection that occurs in a straight channel to become asymmetric about the channel axis.

Time series of the terms in equation (1) are illustrated at depths of 2 and 5 m for a location in the middle of CS2 (see Figure 1a) in Figures 6a and 6b (see also Figure 5b for the location of the point denoted by “+”). The local drivers of lateral flow are the baroclinic pressure gradient force (“bcpgf” in Figures 6a and 6b) and the curvature forcing (“curvf” in Figures 6a and 6b). At both depths examined, these drivers attain comparable magnitudes. Maxima appear during flood and ebb between  $0.4 \times 10^{-4}$  and  $0.9 \times 10^{-4} \text{ m/s}^2$ . According to equation (1), each source term of lateral flow acts in opposite direction near surface and in the deep channel. This is why the time series of “bcpgf” and “curvf” have opposite signs at 2 and 5 m depth (Figures 6a and 6b). The two source terms systematically oppose each other during flood. The individual phases of the tidal cycle are indicated by the vertical dashed lines identifying the times of high water (“HW,” black dashed vertical lines in Figure 6c) and low water (“LW,” gray dashed vertical lines in Figure 6c). Near the surface “curvf” slightly exceeds “bcpgf” whereas near the channel bed the situation is reversed. Lateral currents have no forcing during flood and thus no lateral exchange flow takes place (65 km in Figure 4g). Toward

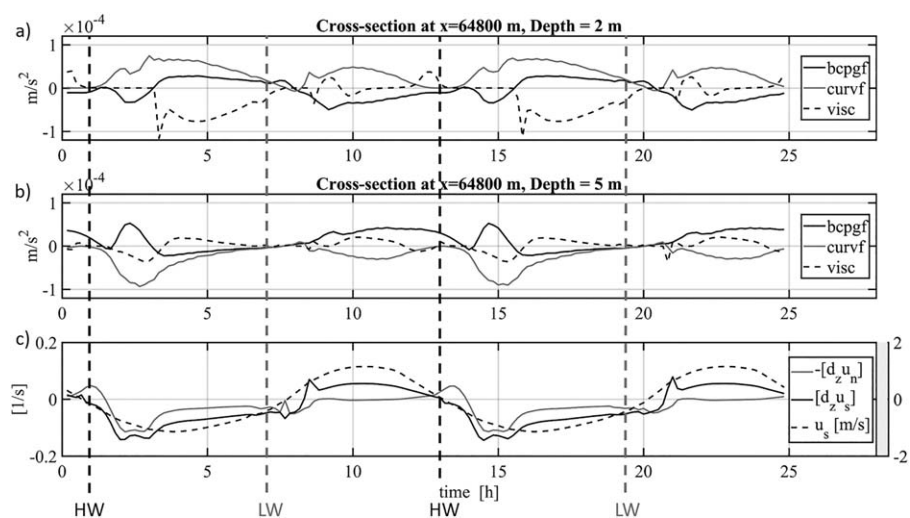


**Figure 6.** Temporal variability of the lateral terms in equation (1) in the middle of CS2 (see Figure 1a) at (a) 2 m and (b) 5 m depth above the bottom (*thalweg*) at a location at 65 km over the *thalweg* in the meandering estuary. Abbreviations represent “visc”—the internal stresses, “bcpgf”—the baroclinic pressure gradient force, “curvf”—the curvature-induced centrifugal force. The cross-channel and along-channel components of the bulk vorticity are illustrated by the gray and black lines in (c), respectively. The along-channel velocity  $u_s$  (m/s) is given by the dashed black line in Figure 6c. The vertical dashed lines indicate the timing of the tidal phases (HW, high water and LW, low water).

high water “curvf” decreases at both depths (high water being by the beginning of ebb in Figures 6a and 6b). On the other hand, “bcpgf” increases at 5 m depth (Figure 6b), i.e., the baroclinic gradients dominate over curvature forcing. It follows that at high water “bcpgf” must drive lateral flow. Within the first hour of ebb “bcpgf” reaches zero indicating that the lateral density gradient has relaxed. The accelerating ebb current (Figure 6c) relates to the acceleration due to “curvf” at 2 and 5 m depth (after 14 h in Figures 6a and 6b). For approximately 90 min, “bcpgf” again opposes “curvf.” After 16 h, i.e., before maximum ebb, “bcpgf” changes sign and supports “curvf” (Figures 6a and 6b). Increased vertical shears of the along-channel velocity during ebb (Figure 3d) lead to maximum curvature forcing (Figures 6a and 6b). The sum of both driving terms leads to the strongest lateral forcing during the tidal cycle. Both terms are balanced by the internal stress, which is represented by “visc” (Figures 6a and 6b).

The degree of coupling between along-channel and lateral flows is illustrated by the time series of bulk along-channel and cross-channel vorticity (Figure 6c). The rotation of the along-channel and cross-channel currents reveals a clear linkage during ebb except the very early ebb. This implies that during most of ebb momentum passes from the along-channel to the cross-channel direction and vice versa. This process is associated with helical flow or lateral exchange flow which is what happens on the meanders of the meandering configuration (see the overturning circulation between 55 and 70 km in Figures 4d, 4f, and 4h). The crucial point is that this mechanism works only at ebb while at flood neither source term of the lateral currents attains dominance nor do the source terms act together.

In summary, two major tidal phases of lateral flows have been discerned: (1) curvature-induced lateral flows at ebb and (2) baroclinically induced flows around high water. During flood, the major drivers of the secondary circulation cancel each other out explaining the asymmetry of the secondary circulation in the meandering channel.

### 3.2.2. Secondary Circulation in Meandering Channels

The secondary circulation is now analyzed at cross section CS2 (see Figure 1). We have demonstrated above that the flood current transports dense water to the inner bends (Figures 5a and 5b). At CS2 the flood-induced salinity difference between the southern (left in Figure 7) and the northern shore amounts to almost 2 g/kg (Figure 7a). The lateral gradients drive the lateral currents toward the northern shore near the channel bed and toward the southern shore near the surface. At the same time, the curvature-induced centrifugal force drives the lateral currents in the opposite direction (Figures 8a and 9b). At high water, the

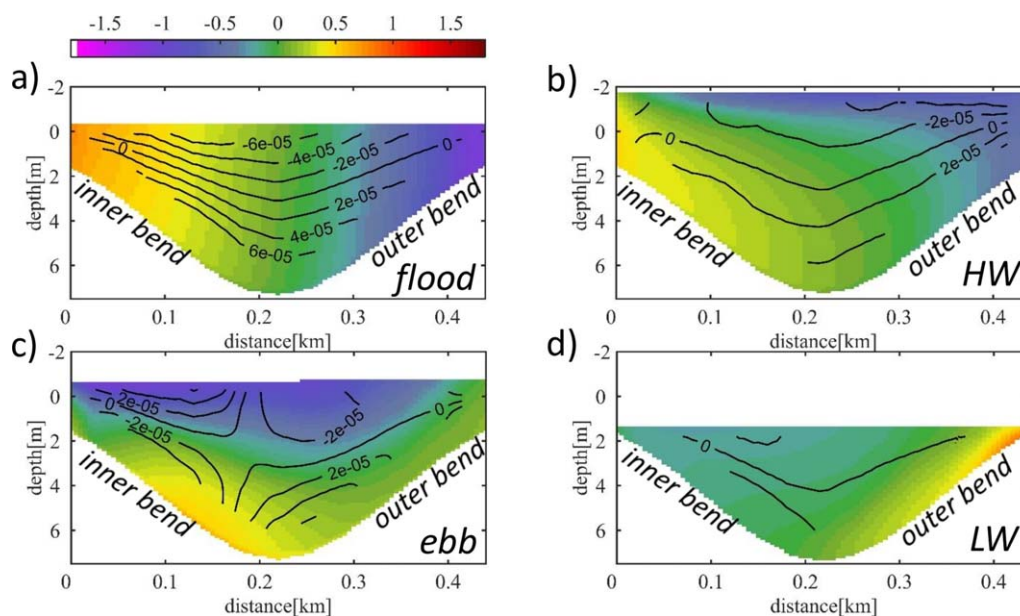


**Figure 7.** Cross-channel sections of the cross-sectional anomaly of salinity (g/kg) for (a) flood, (b) high water, (c) ebb, and (d) low water. The contour lines illustrate the lateral baroclinic forcing ( $\text{m/s}^2$ ) (see also “bcpgf” in Figures 6a and 6c). Looking seaward.

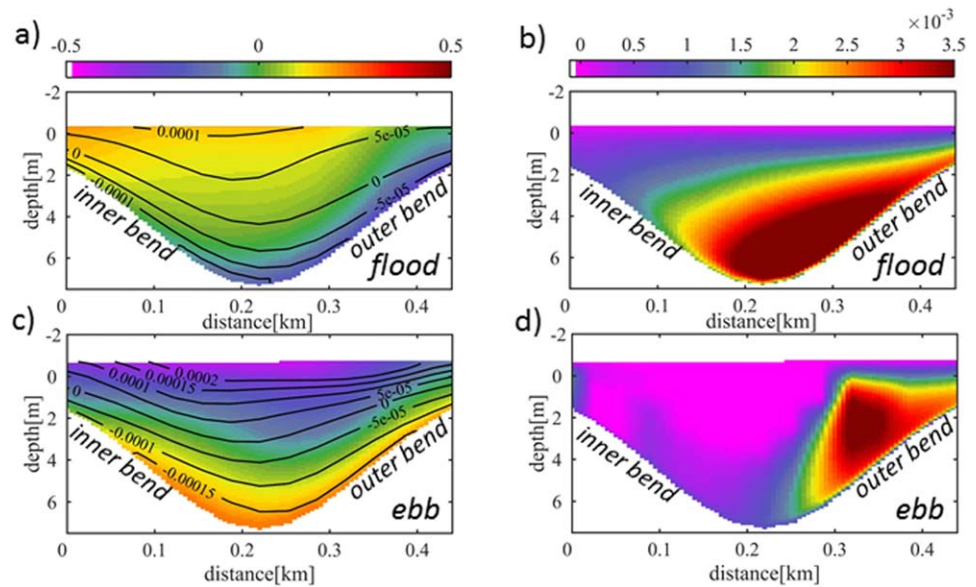


**Figure 8.** Across-channel sections at CS2 (see Figure 1a) of the cross-sectional anomaly of along-channel velocity (m/s) for flood (a) and ebb (c). Contour lines illustrate the curvature-induced centrifugal force (m/s<sup>2</sup>). Across-channel profiles of TKE (J/kg) for flood (b) and ebb (d).

speed of tidal flow approaches zero. As explained with the help of the analysis of the terms of equation (1), the baroclinic gradients at this time drive the lateral currents around high water (Figures 7b, 6a, and 6b).

At ebb, the situation is different from flood. The ebb current brings relatively fresher water to the inner bend setting up a baroclinic forcing toward the outer bend at the surface (Figures 7c and 7d). Figure 7c shows that the lateral salinity maximum is located between the inner bend and the *thalweg* at full ebb setting up opposite baroclinic pressure gradients south and north of this maximum. At full ebb thus, the centrifugal and baroclinic forcing act in concert in the southern part of the channel (0–0.15 km, Figures 7c and 8c). After full ebb, the lateral salinity maximum shifts toward the northern shore such that centrifugal and baroclinic forcing work in the same directions over the whole cross section (Figures 8c, 6a, and 6b). Over the southern part of the channel (inner bend) and the deep channel, TKE reaches about 25% of its flood level (Figures 8b and 8d). Values of TKE attain magnitudes similar to those at flood only in the northern part of the channel and toward full ebb. Near the southern shore tidal straining leads to strong stratification suppressing the TKE locally (between 0.1 and 0.2 km in Figure 7c). Thus, ebb mixing does not fully control the source terms of the lateral circulation (see Figure 8b, 8d, 6a, and 6b). The distribution of the drivers of the secondary circulation in a cross section of the meandering channel revealed the following asymmetries: (1) asymmetry of the balance between baroclinic forcing and curvature forcing; (2) flood-ebb mixing asymmetry associated with (a) control of the secondary circulation by internal stresses and bottom friction at flood and (b) reduced mixing that allows for lateral flows during ebb (Figures 8b and 8d).

Secondary currents at high water and during early ebb are illustrated for cross sections CS1, CS2, CS3, and CS4 (Figure 9, see Figure 1a for their locations). The strongest lateral currents evolve at the bends (Figures 9c–9f; CS2, CS3 in Figure 1a). A single overturning cell appears at the bends at both early ebb and high water. Away from the bends in the landward direction the lateral currents become weaker and lose coherence (Figures 9g and 9h; CS1, CS4 in Figure 1a). In the seaward direction, the overturning circulation extends by several kilometers (Figures 4f and 4h). Between the first and second bends the flow at high water is reminiscent of the gravitational circulation in a straight channel (Figures 9a and 9b; CS1 in Figure 1a) (Burchard et al., 2011; Lerczak & Geyer, 2004). The densest water at CS1 thus appears in the channel's center, whereas in the neighboring bends the lateral density maximum is shifted away from the channel axis toward the inner bend. At the same cross section (CS1), the early ebb current patterns show good agreement with those at the landward bend (CS2), indicating advection of lateral momentum from CS2 to CS1 (Figures 9b and 9d). At the end of the meandering section (CS4), lateral currents show small scale variations with the largest current magnitudes

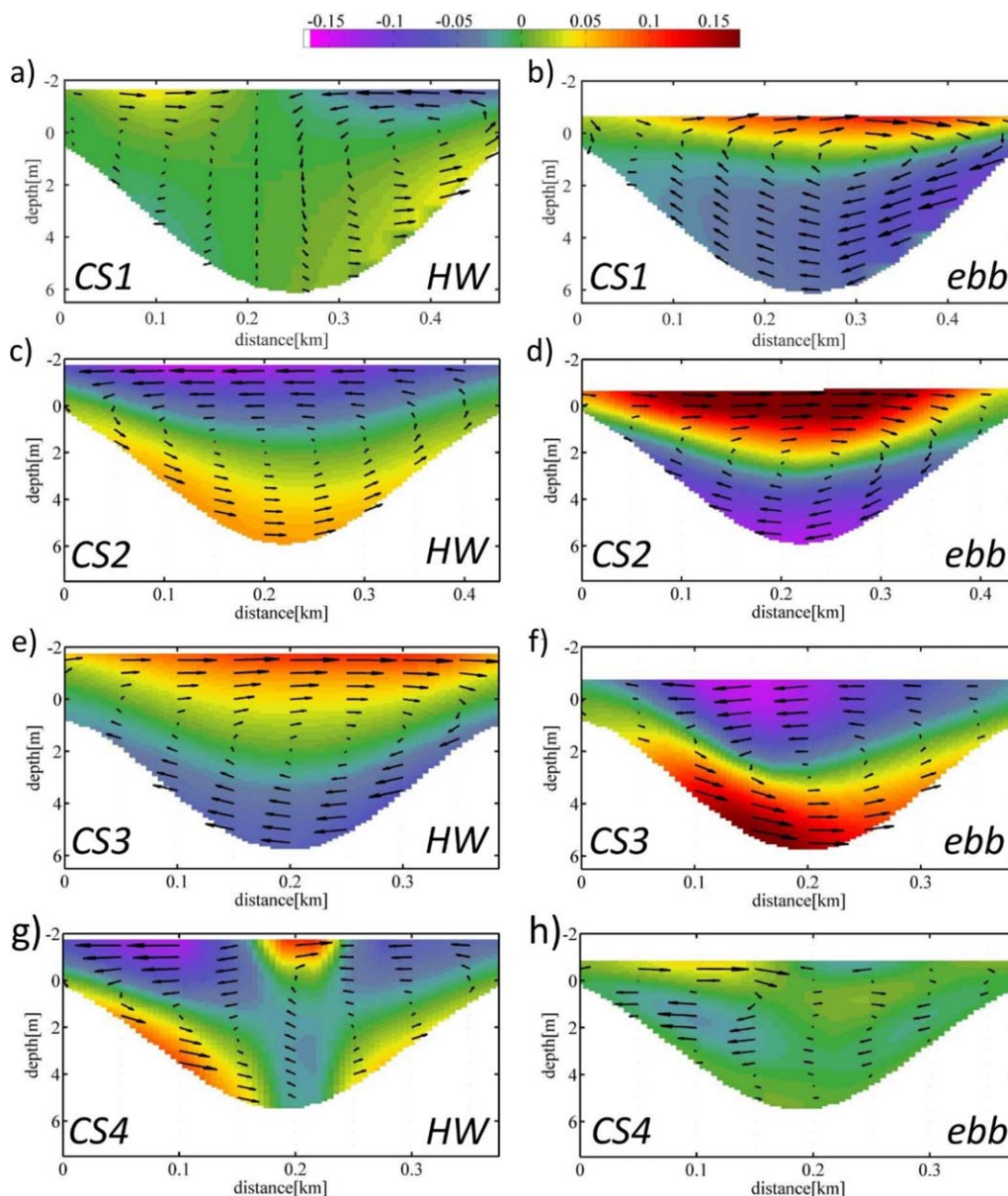


**Figure 9.** Cross sections of the secondary circulation at HW (plots on the left) and during early ebb (plots on the right) along (a, b) CS1, (c, d) CS2, (e, f) CS3, and (g, h) CS4. The colors represent the lateral velocity (m/s). Arrows illustrate the direction of the secondary circulation.

emerging around high water (Figure 9g). At the southern shore, the circulation appears to be driven by the density gradient over the inner side of the bend (Figure 9g, see also Figure 9c). Over the deep channel and the northern shore, the circulation features downwelling of denser water near the center channel (0.23 km in Figure 9g). This cross section thus features both baroclinic regimes, i.e., one observed over the curvature of the channel and one over the deepest part of the straight channel.

#### 4. Conclusions

Several studies have previously addressed the generation of secondary circulation in a single channel bend. This modeling study extended the scope by investigating the lateral dynamics of estuarine flow in several recurrent bend (meanders) along the estuarine salinity gradient. Simulations showed that channel meanders alter the along-channel dynamics, giving rise to higher-order processes in the vertical and lateral

directions. Flood currents were reduced by the friction induced by the meanders. This increase in friction also led to stronger mixing of density in the vertical, which was demonstrated by a reduction of the gradient Richardson number in the region of the meanders (Figure 3k). During ebb, the water column was stratified and the current lost relatively less TKE, compared to flood, by frictional dissipation. Meanders redirected the longitudinal momentum from the principal axis of the flow to the lateral direction (Figure 6c). Also, meanders led to lateral flows that were more than twice greater than the typical differential advection-induced secondary circulation in a straight channel.

A detailed examination of the terms in the lateral momentum equation in one of the meanders revealed asymmetric forcing of the lateral currents in flood and ebb. First, lateral baroclinic gradients and curvature forcing opposed each other at flood. At ebb they mostly reinforced, allowing for the transformation of along-channel momentum into secondary circulation. Second, the flood current was affected by internal stresses and bottom friction in most of the cross-sectional area (Figure 8b). Mixing was the main counterbalance to the forcing induced by curvature and baroclinicity. At ebb, high eddy viscosity (proxy for internal stresses) appeared near the channel wall because of vertically sheared flow. Bottom friction affected only part of the outer bend. Both internal and bottom stresses were damped by stratification. Consequently, turbulence could not break down the secondary flows during ebb.

#### Acknowledgments

The model code that has been used to produce the data analyzed in this paper is available at <http://ccrm.vims.edu/schismweb/>. This study has partially been written in the framework of the Future-Ems project (funding from BMBF, Germany). We want to thank Joseph Zhang (VIMS) for his support with the use of the model. We are also very grateful to Johannes Schulz-Stellenfleth for the fruitful discussions and good advices. We also want to thank Erik Ensing for his help in creating the topography. A.V.L. acknowledges support from NSF projects OCE.

#### References

- Ahnert, F. (1960). Estuarine meanders in the Chesapeake Bay area. *Geographical Review*, 50(3), 390–401.
- Aubrey, D. G., & Speer, P. E. (1985). A study of non-linear tidal propagation in shallow inlet/estuarine systems Part I: Observations. *Estuarine, Coastal and Shelf Science*, 21(2), 185–205.
- Becherer, J., Stacey, M. T., Umlauf, L., & Burchard, H. (2015). Lateral circulation generates flood tide stratification and estuarine exchange flow in a curved tidal inlet. *Journal of Physical Oceanography*, 45(3), 638–656.
- Buijsman, M. C., & Ridderinkhof, H. (2008). Variability of secondary currents in a weakly stratified tidal inlet with low curvature. *Continental Shelf Research*, 28(14), 1711–1723.
- Burchard, H., Hetland, R. D., Schulz, E., & Schuttelaars, H. M. (2011). Drivers of residual estuarine circulation in tidally energetic estuaries: Straight and irrotational channels with parabolic cross section. *Journal of Physical Oceanography*, 41(3), 548–570.
- Burchard, H., & Hofmeister, R. (2008). A dynamic equation for the potential energy anomaly for analysing mixing and stratification in estuaries and coastal seas. *Estuarine, Coastal and Shelf Science*, 77(4), 679–687.
- Dronkers, J. (1996). The influence of buoyancy on transverse circulation and on estuarine dynamics. In D. G. Aubrey & C. T. Friedrichs (Eds.), *Buoyancy effects on coastal and estuarine dynamics* (pp. 341–356). Washington, DC: American Geophysical Union.
- Friedrichs, C. T., Armbrust, B. D., & Swart, H. E. D. (1998). Hydrodynamics and equilibrium sediment dynamics of shallow, funnel-shaped tidal estuaries. In A. Dronkers, & A. Scheffers (Eds.), *Physics of estuaries and coastal seas* (pp. 315–327). Rotterdam, the Netherlands: Balkema.
- Friedrichs, C. T., & Aubrey, D. G. (1988). Non-linear tidal distortion in shallow well-mixed estuaries: A synthesis. *Estuarine, Coastal and Shelf Science*, 27(5), 521–545.
- Geyer, W. R. (1993). Three-dimensional tidal flow around headlands. *Journal of Geophysical Research*, 98(C1), 955–966.
- Giese, B. S., & Jay, D. A. (1989). Modelling tidal energetics of the Columbia River estuary. *Estuarine, Coastal and Shelf Science*, 29(6), 549–571.
- Kalkwijk, J. P. T., & Booij, R. (1986). Adaptation of secondary flow in nearly-horizontal flow. *Journal of Hydraulic Research*, 24(1), 19–37.
- Lacy, J. R., & Monismith, S. G. (2001). Secondary currents in a curved, stratified, estuarine channel. *Journal of Geophysical Research*, 106(31), 283–231.
- Lerczak, J. A., & Geyer, W. R. (2004). Modeling the lateral circulation in straight, stratified estuaries. *Journal of Physical Oceanography*, 34(6), 1410–1428.
- Marani, M., Lanzoni, S., Zandolin, D., Seminara, G., & Rinaldo, A. (2002). Tidal meanders. *Water Resources Research*, 38(11), 1225. <https://doi.org/10.1029/2001WR000404>
- Monismith, S. G. (2010). Mixing in estuaries. In A. Valle-Levinson (Ed.), *Contemporary issues in estuarine physics* (pp. 145–185). Cambridge, UK: Cambridge University Press.
- Nidziedo, N. J., Hench, J. L., & Monismith, S. G. (2009). Lateral circulation in well-mixed and stratified estuarine flows with curvature. *Journal of Physical Oceanography*, 39(4), 831–851.
- Nunes, R. A., & Simpson, J. H. (1985). Axial convergence in a well-mixed estuary. *Estuarine, Coastal and Shelf Science*, 20(5), 637–649.
- Pein, J. U., Stanev, E. V., & Zhang, Y. J. (2014). The tidal asymmetries and residual flows in Ems Estuary. *Ocean Dynamics*, 64(12), 1719–1741.
- Purkiani, K., Becherer, J., Flöser, G., Gräwe, U., Mohrholz, V., Schuttelaars, H. M., et al. (2015). Numerical analysis of stratification and destratification processes in a tidally energetic inlet with an ebb tidal delta. *Journal of Geophysical Research: Oceans*, 120, 225–243. <https://doi.org/10.1002/2014JC010325>
- Rozovskii, I. L. (1957). *Flow of water in bends of open channels*. Kiev, Ukraine: Academy of Sciences of the Ukrainian SSR.
- Seim, H. E., & Gregg, M. C. (1997). The importance of aspiration and channel in curvature in producing strong vertical mixing over a sill. *Journal of Geophysical Research*, 102(C2), 3451–3472.
- Simpson, J. H., Crisp, D. J., & Hearn, C. (1981). The shelf-sea fronts: Implications of their existence and behaviour [and discussion]. *Philosophical Transactions of the Royal Society of London A*, 302(1472), 531–546.
- Talke, S. A., de Swart, H. E., & Schuttelaars, H. M. (2009). Feedback between residual circulations and sediment distribution in highly turbid estuaries: An analytical model. *Continental Shelf Research*, 29(1), 119–135.
- Winterwerp, J. C. (2011). Fine sediment transport by tidal asymmetry in the high-concentrated Ems River: Indications for a regime shift in response to channel deepening. *Ocean Dynamics*, 61(2–3), 203–215.
- Zhang, Y., & Baptista, A. M. (2008). SELFE: A semi-implicit Eulerian-Lagrangian finite-element model for cross-scale ocean circulation. *Ocean Modelling*, 21(3), 71–96.
- Zhang, Y. J., Ye, F., Stanev, E. V., & Grashorn, S. (2016). Seamless cross-scale modelling with SCHISM. *Ocean Modelling*, 102, 64–81.